RSC Advances

ROYAL SOCIETY OF CHEMISTRY

PAPER

View Article Online
View Journal | View Issue

Check for updates

Cite this: *RSC Adv.*, 2024, **14**, 23083

An innovative Schiff-base colorimetric chemosensor for the selective detection of Cu^{2+} ions and its applications†

Ram Kumar,[ab] Bholey Singh, *[c] Parveen Gahlyan,[a] Abhishek Verma,[d] Mamta Bhandari,[e] Rita Kakkar [e] and Balaram Pani *[b]

Received 26th April 2024
Accepted 12th July 2024

DOI: 10.1039/d4ra03097d

rsc.li/rsc-advances

A novel Schiff base moiety, (*E*)-4-(1-hydrazonoethyl)benzene-1,3-diol (**2**), and 2,4-dihydroxybenzaldehyde were condensed in a 1 : 1 molar ratio to generate 4-((*E*)-1-(((*Z*)-2,4dihydroxybenzylidene)hydrazono)ethyl) benzene-1,3-diol (**L**), which was then characterized using high-resolution mass spectrometry (HRMS), ^{1}H-NMR, ^{13}C NMR, and single-crystal XRD techniques. UV-vis absorbance measurements were used to determine whether the Schiff base could detect the cupric ions more effectively than the other transition metal ions. When Cu^{2+} ions were involved, a new band was observed at 462 nm. From the Job plot, the binding stoichiometry for the anticipated **L** : $\mathbf{Cu^{2+}}$ partnership is determined to be 1 : 1. For the purpose of validating structural correlations and absorption data, DFT simulations were performed. Further, docking studies for **L** indicated high binding affinity for human hemoglobin, providing vital information about the ligand's favorable binding locations inside hemoglobin binding sites and the consequent interactions with HHb. The binding coefficient and limit of detection were found to be 3.02×10^{4} M^{-1} and 42.09 nM, respectively. Reversibility of the complex was seen upon the addition of EDTA to the **L–$\mathbf{Cu^{2+}}$** solution, and a colorimetric variation simulating the "INHIBIT" molecular logic gate was seen upon the addition of Cu^{2+} and EDTA to **L**. Furthermore, the chemosensor's potential application in the detection of Cu^{2+} in the solid state by chemosensor **L** also confirms its usefulness in real-world applications emphasizing its versatility and practical utility.

1. Introduction

Cu^{2+} is a vital trace element for human health and plays an important role in the production of several enzymes, cell metabolism, and other biochemical processes. However, excessive Cu^{2+} has harmful effects on human health and the environment, particularly the amplifying effect of the biological chain, which can be enriched multiple times, eventually entering the human body[1,2] and causing damage to the central nervous system including Alzheimer's, Parkinson's, and prion diseases.[3] Therefore, the detection of Cu^{2+} is important for environmental monitoring and healthcare issues. Cu^{2+} levels in drinking water should be less than 31.5 M, according to the World Health Organization (WHO).[4–6] A number of conventional techniques have been developed over the years to identify metal ions, including inductively coupled plasma spectroscopy, atomic absorption spectroscopy, and inductively coupled plasma mass spectrometry.[7–10] In addition to these approaches, impedimetric sensing and electrochemical monitoring have also been mentioned in recent publications on the detection of Cu^{2+}.[11–14] These techniques provide precise results for the detection of metal ions; however, they have significant practical limitations owing to the high cost of equipment, difficulty of the procedures, and length of inspections.[15–17] There are several important reasons for the importance of detecting copper. It may also be noted that copper is considered an "economically critical mineral" due to its importance for a variety of important technologies.[18–20] Having low-cost, sensitive, selective, and portable sensors for characterizing copper could therefore be useful for both prospecting and downstream process monitoring during copper production, especially from unconventional sources such as industrial waste.[21,22]

However, there is an urgent need to develop quick, trustworthy, inexpensive, and straightforward measurement techniques, including electrochemical and optical sensing methods, for practical applications, particularly rapid on-site detection of metal ions. In the present investigation, we have

---

[a] Department of Chemistry, University of Delhi, Delhi 110007, India

[b] Department of Chemistry, Bhaskaracharya College of Applied Sciences, University of Delhi, New Delhi 110075, India. E-mail: balarampani63@gmail.com

[c] Department of Chemistry, Swami Shraddhanand College, University of Delhi, Delhi 110036, India. E-mail: bholeysingh@ss.du.ac.in

[d] Department of Chemistry, Kirori Mal College, University of Delhi, Delhi 110007, India

[e] Computational Chemistry Group, Department of Chemistry, University of Delhi, Delhi 110007, India

† Electronic supplementary information (ESI) available. CCDC 2296396. For ESI and crystallographic data in CIF or other electronic format see DOI: https://doi.org/10.1039/d4ra03097d

created a Schiff base moiety based on 2,4-dihydroxy benzaldehyde that acts as a colorimetric chemosensor. We employed different types of metal ions as analytes to demonstrate how this technique can be used to selectively determine Cu^{2+}. The synthesized novel chemosensor **L** displayed remarkable sensitivity and selectivity for Cu^{2+} ions over other metals forming a stable combination with Cu^{2+} ions, resulting in a visible color shift making it a promising tool for environmental monitoring and analytical applications. Additionally, the findings from the computational and practical investigations contribute to a greater scientific understanding of protein–ligand interactions, opening the way for advances in domains such as pharmacology, biochemistry, and molecular biology.

2. Experimental

2.1 General information, materials and methods

For synthesis and spectroscopic investigations, exclusively reagent-grade chemicals and solvents were used. The following ingredients were purchased from Spectrochem Pvt. Ltd (India): 1-(2,4-dihydroxyphenyl)ethan-1-one, hydrazine hydrate, ethanol, and 2,4-dihydroxy benzaldehyde. Further purification was not required to perform the reaction. To conduct spectroscopic studies, stock solutions of metal ions were prepared in double-distilled water. Chloride salts of Cu^{2+}, Co^{2+}, Cr^{3+}, Cs^{+}, Fe^{2+}, Fe^{3+}, In^{3+}, K^{+}, Li^{+}, Mg^{2+}, Na^{+}, Ni^{2+}, Zn^{2+}, Hg^{2+}, Mn^{2+}, and Cd^{2+}, nitrate salts of Ag^{+}, Pb^{2+} and sulphate salt of Al^{3+} were obtained from Spectrochem Pvt. Ltd and were utilized as received. Column chromatography (silica gel, 100–200 mesh) with methanol–chloroform as the solvent system was used to purify the chemicals. Thin-layer chromatography (Merck silica gel 60F 254) was used to monitor the completion of the reaction. Fourier transform infrared (FT-IR) spectra were obtained using a SHIMADZU IR Affinity 1S spectrophotometer. A JNM-EXCP 400 (JEOL, USA) spectrophotometer was used to record nuclear magnetic resonance (NMR) spectra at room temperature while operating at 400 MHz and 100 MHz. A single-sided transparent glass capillary tube was used to record the melting point of the compound using a Buchi M-560 melting point device. An Agilent Technologies G6530AA (LC-HRMS-Q-ROF) spectrometer was used to record high-resolution mass spectrometry (HRMS) spectra. A Rigaku Oxford diffraction instrument was used for crystal analysis. A Cary Series UV-visible spectrophotometer was used for UV-visible investigations using a 1 cm quartz cuvette. The pH was measured using a digital pH meter.

2.2 Synthesis

2.2.1 Synthesis of (*E*)-4-(1-hydrazonoethyl)benzene-1,3-diol (2). 1-(2,4-Dihydroxyphenyl)ethan-1-one (**1**; 1 g; 6.5 mmol) and excess hydrazine hydrate were dissolved in 50 mL ethanol and refluxed for 6 h. The reaction mixture was transformed into an oily residue. The residue was dissolved in hexane (100 mL) and cooled. Filtration was used to separate the crystalline product, which was then washed with petroleum ether five times and dried in air to produce a pure product with a yield of 90%.

2.2.2 Synthesis of 4-((*E*)-1-(((*Z*)-2,4-dihydroxybenzylidene)hydrazono)ethyl)benzene-1,3-diol (L). A solution of (*E*)-4-(1-hydrazonoethyl)benzene-1,3-diol (**2**; 0.50 g, 3.012 mmol) in ethanol was gently mixed with a solution of 2,4-dihydroxybenzaldehyde (0.415 g, 3.012 mmol) in ethanol. At 80 °C, the reaction mixture was stirrer for 4 h and monitored by thin-layer chromatography (TLC). The resulting white solution was evaporated at room temperature. A white precipitate formed after the addition of anhydrous ether. The resulting residue was repeatedly washed with cold ethanol before recrystallization from ethyl acetate and dried *in vacuo* over anhydrous $CaCl_2$. The sensor **L** obtained is 82% yield and m.p. was observed to be 127–130 °C, ^{1}H NMR (400 MHz, DMSO-d_6): δ (ppm) 13.5 (s, 1H, –OH), 11.3 (s, 1H, –OH), 10.2 (s, 1H, –OH), 10.06 (s, 1H, –OH), 8.7 (s, 1H, –CH), 7.51 (s, $J = 7.50$ Hz, 1H, Ar–H), 7.46 (d, $J = 7.43$ Hz, 1H, Ar–H), 6.37 (s, 1H, Ar–H), 6.36 (d, $J = 6.34$ Hz, 1H, Ar–H), 6.31 (d, $J = 6.34$ Hz, 1H, Ar–H), 6.23 (d, $J = 6.30$ Hz, 1H, Ar–H), 2.45 (s, 3H, C–H). ^{13}C-NMR (100 MHz, DMSO-d_6) δ 168.89, 162.74, 162.46, 161.93, 161.19, 160.76, 133.32, 131.60, 111.69, 111.18, 108.86, 107.99, 103.46, 102.91, 14.64. HRMS: calculated for $C_{15}H_{14}N_2O_4$ $[M + H]^+$ 287.40; obtained 287.42.

2.3 Single crystal X-ray diffraction analysis

Fine crystals of ligand **L** were grown by slow evaporation of the saturated mother solvent methanol, which was layered with hexane at room temperature for SC-XRD studies. Good quality needle-shaped transparent crystals were obtained and exposed to X-rays on a Bruker diffractometer employing graphite monochromatized Mo Kα radiation ($\lambda = 0.71073$ Å) at a temperature of 107 K. The crystal data were reduced using the CrysAlis Pro software available with the diffractometer. Further, least-squares refinement after the introduction of anisotropic displacement parameters yielded the *R* values mentioned in Table S1 (ESI).† The structure was solved by direct methods using SHELXT 2018/2 (ref. 23) and refined using the full-matrix least-squares method on Olex2.refine 1.5, and SHELXL-2016/4. All calculations were performed using the OLEX2 package of crystallographic programs.[24] For molecular graphics, the Mercury program (2022.3.0) was used.[25] The selected cell parameters are listed in Table S1 (ESI).†

2.4 UV-visible studies

UV-visible studies have been carried out to investigate the binding behavior of **L** towards various metal ions. An initial stock solution of **L** (1 mM) was prepared in acetonitrile, and stock solutions of ethylenediaminetetraacetic acid (EDTA) and metal ions (Ag^{+}, Cu^{2+}, Al^{3+}, Co^{2+}, Cr^{3+}, Cs^{+}, Fe^{2+}, Fe^{3+}, In^{3+}, K^{+}, Li^{+}, Mg^{2+}, Na^{+}, Ni^{2+}, Pb^{2+}, Zn^{2+}, Hg^{2+}, Mn^{2+}, and Cd^{2+}) (10 mM) were prepared in double-distilled water. Chemosensor **L** solution (10 μM) was prepared in CH_3CN for binding studies. In a cuvette, 2.97 mL of **L** (10 μM) was combined with 30 μL of the metal ion stock solution. The UV-visible spectra of probe **L** were recorded in the presence and absence of various metal ions.

2.5 Selectivity

Competitive studies were carried out by adding a variety of metal ions to a solution of Cu^{2+} to evaluate the potential interference by other metal ions in the detection of Cu^{2+}. By mixing equal parts of **L** and metal salts in a quartz cuvette, solutions were created to monitor UV-visible changes.

2.6 Binding and stoichiometric calculations

Benesi–Hildebrand (B–H) and Job's plots, respectively, were used to calculate the binding constant (K_a) for the formation of the complexes and the stoichiometry of the complex of Cu^{2+} with chemosensor **L**. Eqn (1) was used to determine the binding constant from the slope of the B–H plot.

$$\frac{1}{A - A_0} = \frac{1}{K_a(A_{\max} - A_0)C} + \frac{1}{(A_{\max} - A_0)} \tag{1}$$

In eqn (1), A_o and A are the absorbances in the absence and presence of Cu^{2+}, respectively, C represents the amount of Cu^{2+} supplied during the titration, and $A_{\max}$ is the highest absorption intensity recorded.

Eqn (2) was used to determine the limit of detection (LOD) of Cu^{2+}.

$$\text{LOD} = \frac{3\sigma}{K_a} \tag{2}$$

where K_a was determined from the slope of the B–H plot and σ is the standard deviation of the blank solution. The binding stoichiometry for the production of the complexes was determined using Job's plot. Stock solutions of **L** and Cu^{2+} were prepared at a concentration of 10 μM. To keep the final volume at 3 mL, further additions of 0.3–2.7 mL of Cu^{2+} and 2.7–0.3 mL of **L** were made, respectively, in a quartz cuvette. To identify the mole fraction at which the concentration of the complex was greatest, a Job's plot was generated by plotting the mole fractions of **L** (X_R) *vs.* $(A - A_o) \times$ **L**.

2.7 Computational methods

Molecular docking studies were employed to analyze the binding interactions between ligand **L** and hemoglobin (Hb) to elucidate potential therapeutic implications or physiological effects. Hemoglobin is a tetrameric protein found in red blood cells (RBCs) that transports oxygen from the lungs to tissues.[26] Understanding how they bind to different ligands is critical for drug development. In this study, we used molecular docking to investigate the probable binding of ligand **L** to Hb. The three-dimensional crystal structure of human hemoglobin (PDB ID: 2d60) was retrieved from the protein databank. Any water molecules, co-crystallized ligands, or ions were eliminated and hydrogen atoms that were absent were added. Molecular docking assessments were performed for **L** with human hemoglobin using AutoDock Vina software.[27] Grid parameters were chosen to include probable binding locations on the hemoglobin structure. PYMOL and BIOVIA Discovery Studio 2021 were employed to visualize the protein–ligand complex, and the conformer with the lowest binding energy was chosen for diagrammatic representation.

Quantum chemical calculations are valuable tools for predicting equilibrium geometries of metal–ligand complexes. Density functional theory (DFT) calculations were performed using the B3LYP functional.[17–20] All atoms were described using the 6-31G+(d,p) basis set, whereas heavy atoms were treated using the LanL2DZ basis set.[21–24] The ligand and its complex were geometrically optimized *in vacuo* with respect to energy using the Gaussian 09 W suite,[25] followed by harmonic frequency calculations to confirm the nature of the stationary points.

3. Result and discussion

3.1 Synthesis

The colorimetric sensor was prepared by stirring a solution of (*E*)-4-(1-hydrazonoethyl)benzene-1,3-diol and 2,4-dihydroxybenzaldehyde in ethanol (Scheme 1). To generate final product as sensor **L**, the reaction mixture was refluxed for 6 h. The stated procedure was used to generate the precursors **2** of the final product.[28] The spectroscopic methods that such as ^1H NMR, ^{13}C

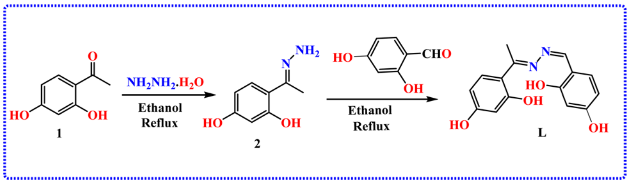

Scheme 1 Synthesis of chemosensor L.

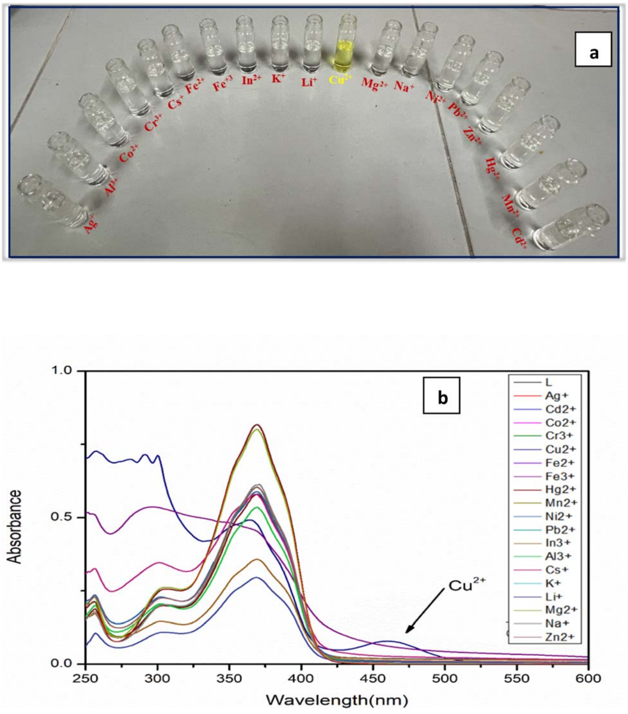

Fig. 1 (a) Visual color changes of L (10 μM, CH_3CN, pH 7.5) towards Cu^{2+} ions. (b) After adding 10 equivalents of various metal ions to L (10 μM, CH_3CN, pH 7.5), the resulting UV-visible spectrum is presented.

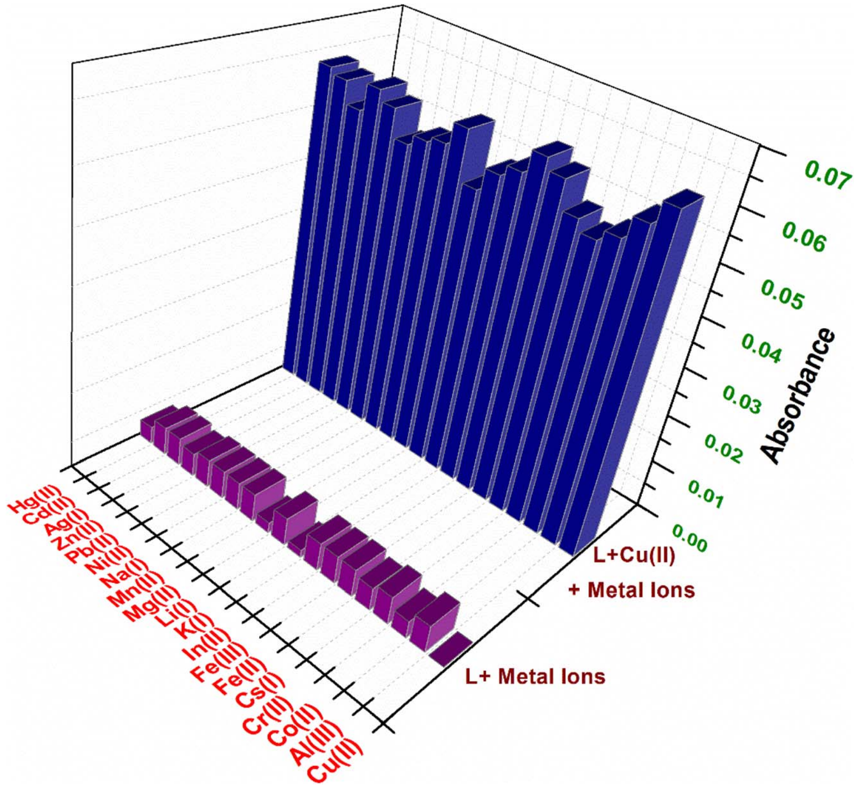

Fig. 2 3D representation of the selectivity of **L** (10 μM, CH_3CN) for Cu^{2+} in the presence of different metal ions at a wavelength of 462 nm.

NMR, IR, and HRMS were used to validate the existence of the final product and its predecessors.

3.2 UV-vis spectral analysis

In order to acquire a more comprehensive understanding of the detecting capabilities of chemosensor **L**, we performed investigations such as UV-visible titration. At a concentration of 10, the UV-visible absorption spectrum of **L** was examined in acetonitrile solution and the pH of the solution was 7.5. The chemosensor didn't show any visible bands when 10 equivalent of metal ions (Ag^+, Cu^{2+}, Al^{3+}, Co^{2+}, Cr^{3+}, Cs^+, Fe^{2+}, Fe^{3+}, In^{3+}, K^+, Li^+, Mg^{2+}, Na^+, Ni^{2+}, Pb^{2+}, Zn^{2+}, Hg^{2+}, Mn^{2+}, and Cd^{2+}) were introduced to the solution of **L**. The only exception to this was the Cu^{2+} case and new band emerged at 462 nm, which is shown in Fig. 1b.

3.3 Selectivity

Equal concentrations of Cu^{2+} and other metal ions were used to check the selectivity, and competitive experiments were carried out to investigate the interference of other metal ions in the detection of Cu^{2+}, as shown in Fig. 2. The color changed from colorless to yellow when Cu^{2+} was added to a solution of **L**, which already contained other metal ions, and the experiment revealed that the UV-visible spectrum of **L** contained Cu^{2+}.

3.4 pH Analysis

The colorimetric response of **L** was investigated as a function of pH in the presence and absence of Cu^{2+}. 1 M sodium hydroxide (NaOH) and 1 M hydrochloric acid (HCl) solutions were added to the mixture to regulate pH. As shown in Fig. 3, protonation at pH 3 prevented the detection of Cu^{2+}. The sensing capacity of **L** for Cu^{2+} increased with pH and then became nearly constant at pH 8. Therefore, it can be concluded that the chemosensor is appropriate for detecting Cu^{2+} under physiological pH conditions.

3.5 Time dependent UV-vis spectra of L and L + Cu^{2+}

To examine the UV-visible absorbance response of the chemosensors **L** and **L** + Cu^{2+} at 462 nm with regard to time, a time-

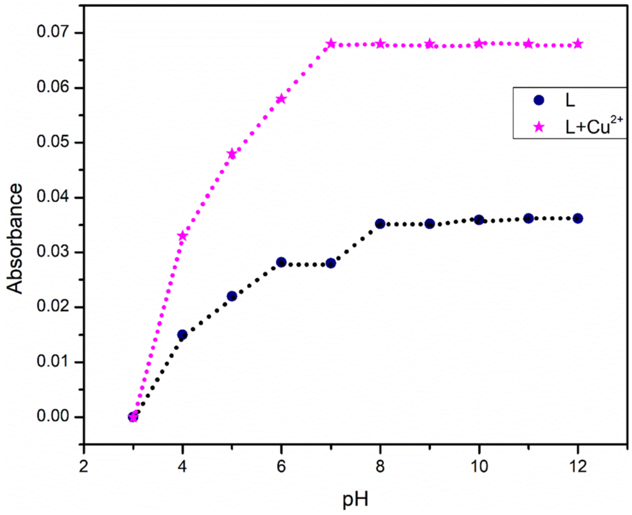

Fig. 3 Impact of pH on the absorption intensity of **L** at 462 nm.

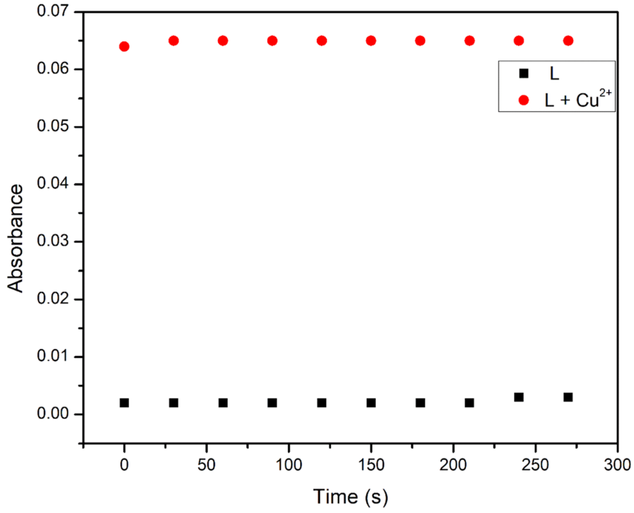

Fig. 4 Absorbance response of L (CH_3CN, pH 7.5) at 462 nm in the presence of 1 equivalent of Cu^{2+}.

dependent investigation of **L** was also carried out. When 1 equivalent of Cu^{2+} ions were added to the solution, the absorbance of **L** (10 μM) at 462 nm increased within a few seconds and remained constant throughout the time, as can be observed in Fig. 4. Therefore, probe **L** can be used for the rapid and precise detection of Cu^{2+} ions.

3.6 Binding stoichiometry ratio analysis

To better understand the binding affinity of chemosensor **L** for Cu^{2+}, a UV-visible titration experiment was conducted in CH_3CN at pH 7.5. As Cu^{2+} was gradually added to the solution of **L**, as shown in Fig. 5a, the absorbance intensity steadily increased in the UV-Vis spectra. Furthermore, the binding constant and stoichiometry of the complex were determined using Job's and Benesi–Hildebrand (B–H) plots, respectively. At a 0.5 mole ratio of **L** to Cu^{2+}, the maximum was observed in the Job's plot (Fig. 5b). Thus, **L** and Cu^{2+} have a 1 : 1 binding stoichiometry and this binding stoichiometry of the complex was further confirmed by the linearity of the B–H curve (Fig. 5c), with an R^2 value of 0.99428. Using the Benesi–Hildebrand plot, it was calculated that the binding constant (K_a) of **L** for Cu^{2+} was $3.02 \times 10^4\ M^{-1}$. The limit of detection (LOD) of chemosensor **L** for Cu^{2+} is 42.09 nM (Table S4 ESI†). This suggests that chemosensor **L** can be utilized to detect Cu^{2+} quantitatively, even at nano-level concentrations. In addition to this, we conducted the infrared spectroscopy experiments also to validate the **L**–Cu^{2+} complex formation as shown in Fig. S7.† It is clearly visible in the IR spectrum that –C═N stretching frequency at 1662 cm^{-1} in free ligand is shifted to 1645 cm^{-1} in the **L**–Cu^{2+} complex and the –OH band at 3321 cm^{-1} in the uncomplexed **L** has been slightly shifted to 3310 cm^{-1} in the complex with increased of broadness. The IR frequencies changes validate the complex formation through –C═N and phenolic –OH groups.

Sensor **L** shows outstanding sensing ability for Cu^{2+} ions as compared to many reported studies, as shown in Table 2.

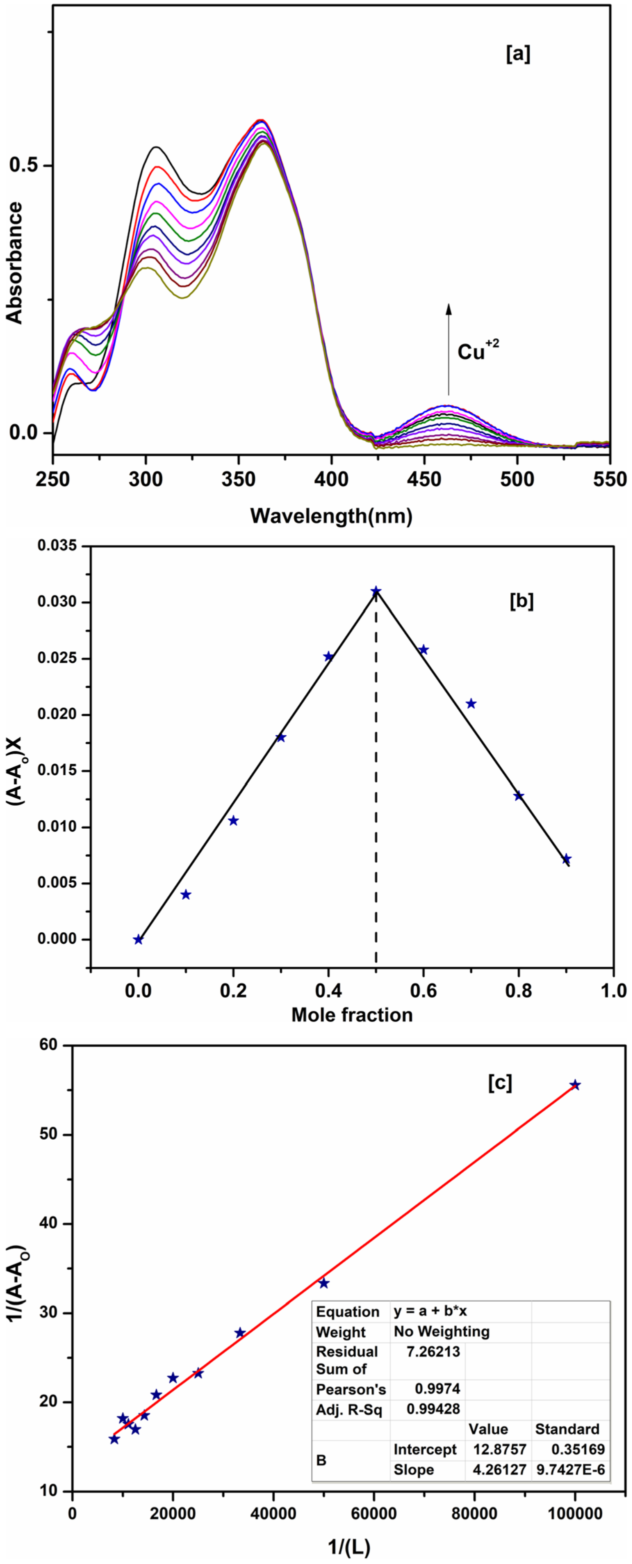

Fig. 5 (a) Absorbance spectra of L (10 μM, CH_3CN, pH 7.5) upon the addition of Cu^{2+} metal ions. (b) Job plot of L for Cu^{2+}. (c) B–H plot of L for Cu^{2+}.

3.7 Single crystal X-ray diffraction analysis

The crystal structure of ligand **L** was determined by the single-crystal X-ray diffraction method, which revealed that the

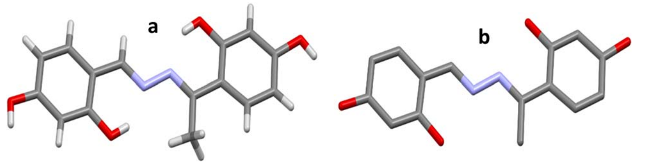

Fig. 6 Molecular structures (a and b) of ligand **L**. H atoms are omitted from b for clarity. C, gray; N = blue, O, red; H, light gray.

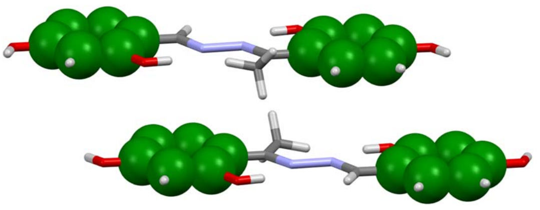

Fig. 7 Double-decker π-stacked arrangement of phenyl rings between adjacent molecules.

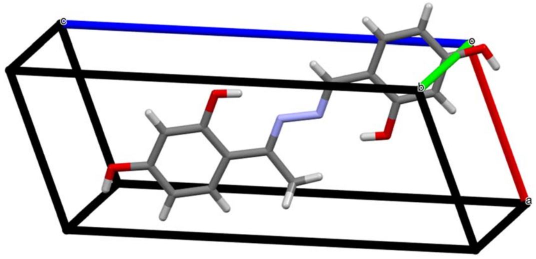

Fig. 8 3D packing arrangement of the cell axis passing through the molecule.

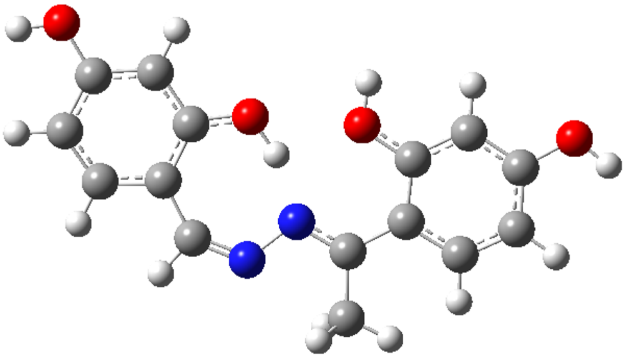

Fig. 10 Optimized geometry of ligand **L**.

molecular structure of the ligand consisted of two dihydroxy aryl rings that were skewed and coordinated with the next carbon atoms at 121.56°and 121.79°, respectively, and supported by the vertically appended methyl group with an imine functional group at an angle of 116.92°. This confirms the planar structure of the compound, which is clearly shown in Fig. 6, where the bond distances of adjacent atoms from the dihydroxy aryl ring to carbon atoms lie in the range 1.443(2)–1.463(2) Å, whereas the inter- and intra-molecular hydrogen and covalent bond lengths lie close to (1.888–2.682 Å). The fundamental building blocks of crystal engineering are weaker coordinating connections, which are crucial. Interestingly, the crystal structures of ligand **L** in the current study showed a variety of non-covalent interactions, including a network of intermolecular H-bonding and π–π stacking configurations (Fig. 7–9). These non-covalent interactions are responsible for different biological applications, such as interactions with hemoglobin protein and metal sensing, where molecules interact in the form of loose aggregates to form metal complexes, as confirmed by molecular docking studies and DFT calculations.

3.8 Computational results

3.8.1 DFT computations

3.8.1.1 Ligand (L). The optimized geometry of the ligand is shown in Fig. 10. It is planar and has C_s symmetry with a $^1A'$ ground state.

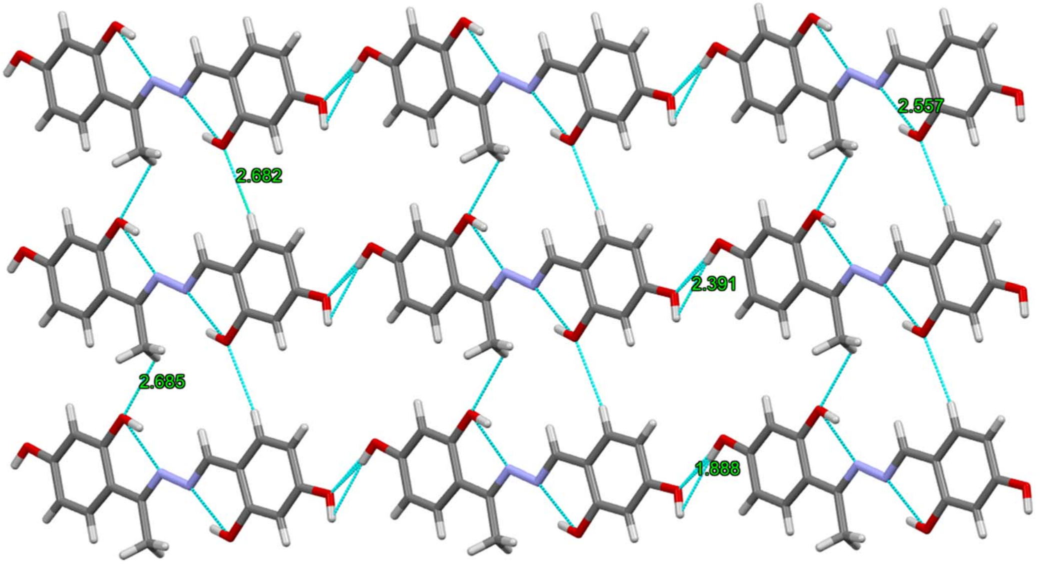

Fig. 9 Network of ligand **L** *via* intra- and intermolecular H-bonding between adjacent molecules.

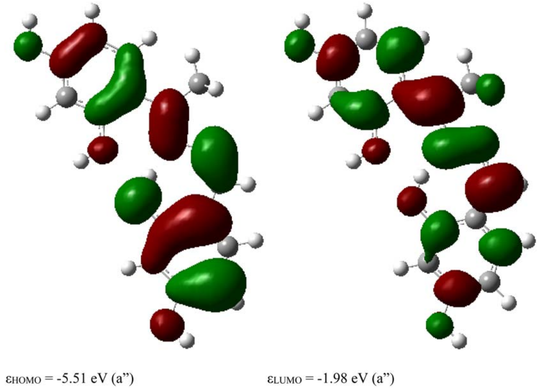

Fig. 11 HOMO and LUMO of ligand (**L**).

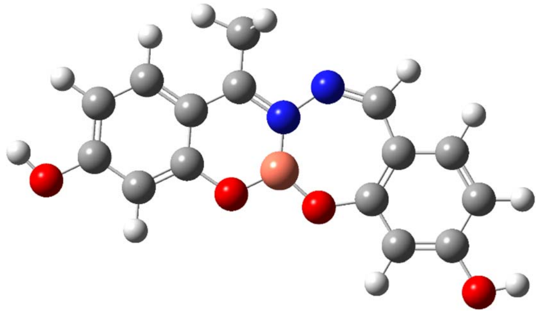

Fig. 12 Optimized structure of the **L**–Cu^{2+} complex.

The highest occupied and lowest unoccupied molecular orbitals (HOMO and LUMO, respectively) are shown in Fig. 11. These are π and π* orbitals, respectively, both of which have a'' symmetry.

3.8.1.2 Cu^{2+} complex. The optimized structure of the complex is shown in Fig. 12. Similar to the ligand, the complex is planar (C_s symmetry), with the Cu^{2+} ion bound to three atoms: two oxygens of the deprotonated hydroxyl groups and an imine nitrogen atom, forming six- and seven-membered rings. The ground state is a doublet.

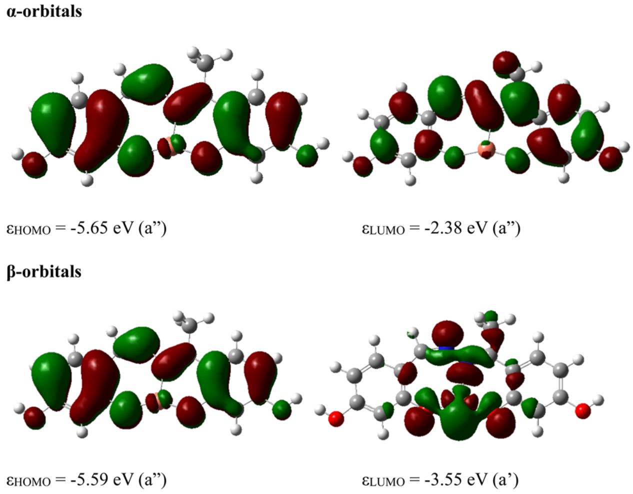

Fig. 13 HOMOs and LUMOs for the two spin states.

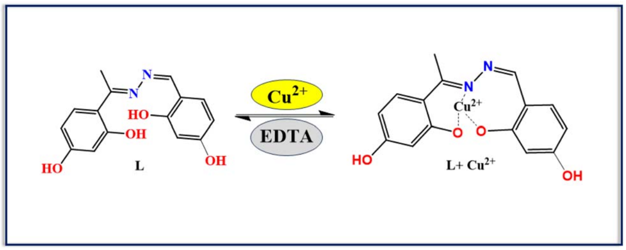

Scheme 2 Plausible mechanism and binding behavior of Cu^{2+} ions to **L** and reversibility of **L** with Cu^{2+} and EDTA.

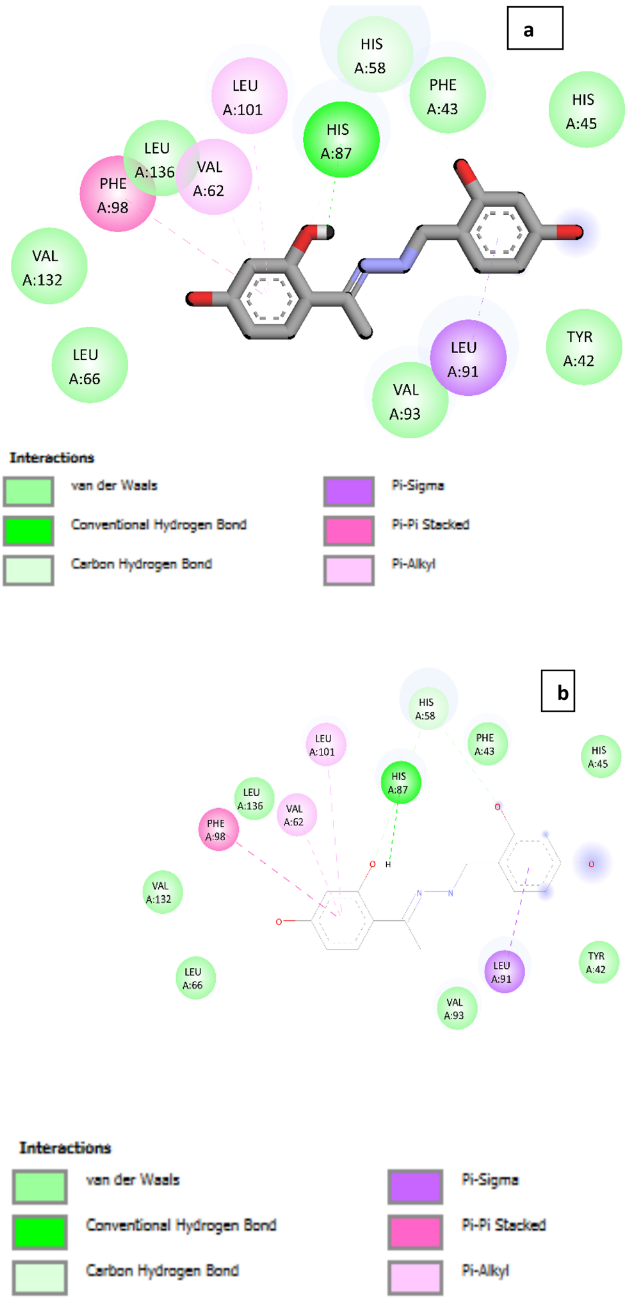

Fig. 14 (a and b): 2-D representation of binding interaction of **L** with human hemoglobin (PDB ID: 2d60).

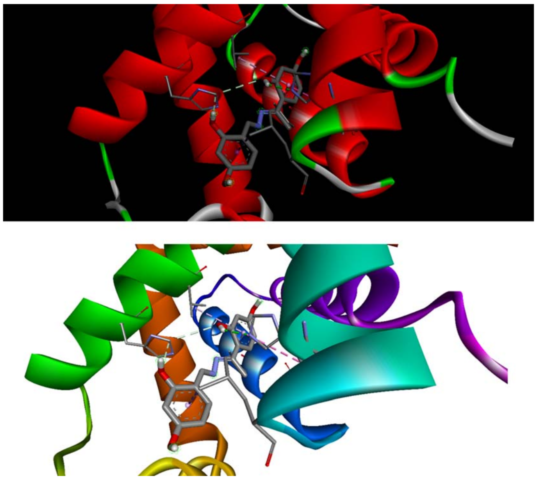

Fig. 15 3-D representation of binding interaction of **L** with human hemoglobin (PDB ID: 2d60).

The HOMO and LUMO of the α and β orbitals are shown in Fig. 13. Although the HOMO is MO#84 for the α-spin state and MO#83 for the β-spin state, the two HOMOs are similar for the two spin states and have similar energies.

The HOMOs are also similar to those of the ligand in terms of energy and appearance, but the LUMO energies are lowered upon complexation with Cu^{2+}, indicating that the electron affinity increases. The LUMO of the β orbitals has a different appearance and involves the d orbitals of the metal ion. It is also symmetric (a') as opposed to the other frontier orbitals.

The Mulliken spin densities are distributed in the central portion of the complex, mainly on the Cu^{2+} ion (0.500), two oxygen atoms (0.147 and 0.132), and imine nitrogen (0.158), to which the metal ion is attached (Fig. 6 ESI†).

The decrease in the HOMO–LUMO gap upon complexation explains the appearance of a band in the visible region upon complexation with Cu^{2+}. TD-DFT calculations were performed for the ligand and complex. The results for the first six excited states of ligand **L** are presented in (Table S2 ESI†).

The observation of these two peaks is in agreement with the experimental observation of the two peaks at 304 and 370 nm (Fig. 4 ESI†). Both transitions are π–π* transitions.

The computed spectrum after complexation is shown in (Fig. 5 in ESI†), and selected transitions for which the oscillator strength is nonzero are given in (Table S3 ESI†).

The highest value of oscillator strength was calculated for transition#10 at 444 nm, in agreement with the experimental results. This transition is the HOMO → LUMO transition of the α-electrons.[29–33] We propose a plausible mechanism for the binding of Cu^{2+} to **L** (Scheme 2).

3.8.2 Docking results. The docking results were examined to determine the most favorable binding positions of the ligand within the hemoglobin binding sites. To evaluate the strength of the ligand–protein interactions, the binding affinity was obtained along with the determination of hydrogen bonds and hydrophobic interactions. A remarkable binding affinity of -7.5 kcal mol^{-1} was achieved for the interaction of the binding sites of human hemoglobin (HHb) with ligand **L**, indicating its excellent binding and potential interactions with HHb. As evident from Fig. 14, the dihydroxybenzyl ring B exhibits π–σ interactions with LEU91. Dihydroxybenzyl ring A is involved in π-alkyl interactions with the amino acid residues LEU101 and VAL62, along with π–π stacked interactions with PHE98. Furthermore, this ligand also exhibits hydrogen bonding interactions with HIS87 and HIS58, and a number of van der Waals interactions with amino acid residues HIS45, PHE43, TYR42, VAL93, LEU66, VAL132, and LEU136. Fig. 15 shows a three-dimensional representation of the binding interaction between **L** and HHb. Docking investigations for **L** demonstrated excellent binding affinity with human hemoglobin, revealing valuable insights into the binding interactions between the ligand and HHb.

4. Practical applications

4.1 Detection of Cu^{2+} ions in solid media using L

The solid-state detection of Cu^{2+} was performed to assess the practical usefulness of **L**. A 100 μM solution of **L** in acetonitrile was mixed with 300 mg of silica gel (100–200 mesh size) for this experiment, the solution of **L** was evaporated under vacuum to produce colorless silica gel. The resulting colorless silica gel was then administered a dose of Cu^{2+}. Subsequently, the water was evaporated, leaving behind yellow silica gel. This demonstrates the colorimetric detection of **L** towards Cu^{2+} in a solid medium, which can be clearly seen in Fig. 16. The chemosensor **L** binds to the silica gel through physical adsorption. Silica gel possesses a remarkable surface area and porous structure that enables the adsorption of chemosensor **L** molecules onto its surface. This interaction is mainly influenced by the attractive forces between molecules and the bonding between different functional groups. The binding stability of chemosensor **L** on silica gel is more than enough for practical colorimetric detection under laboratory conditions. However, to ensure long-term stability and adaptability to different environmental conditions.

4.2 Application of strip filters

This experiment employing paper strips is a crucial application of chemosensor **L** because it can detect ions without the use of

Fig. 16 Silica gel showing the colorimetric response of **L** (100 μM in acetonitrile) towards Cu^{2+} ions in a solid medium.

any technical methods. As a result, it speeds up the detection and simplifies the recognition process. A strip of Whatman filter paper was dipped into an acetonitrile solution of **L** and air-dried to conduct this test. The coated paper strips were submerged at various concentration of Cu^{2+} ions in aqueous solution. The hue shifted from light yellow to dark yellow as the quantity of Cu^{2+} increased, as observed by the naked eye (Fig. 17). This technique is very helpful for on-site detection of ambient condition.

4.3 Detection of Cu^{2+} in real water sample

An investigation into the practicability of using the **L** as a probe to detect Cu^{2+} in real water samples was carried out in order to obtain the results of the feasibility study. In order to conduct this investigation, samples of water from the Ganga river, the Yamuna river, and the tap water were utilised. Before starting with the analysis of the target analyte ($Cu^{2+)}$ at the most appropriate pH conditions, the water samples were first filtered in order to remove any particles that were suspended in the water. There is a preferential binding of the probe **L** with the Cu^{2+} ions that are present in the river water samples. This result illustrates that it is possible for us to determine the presence of copper in the sample in a short amount of time (Fig. 18).

Further, the effectiveness of the probe **L** was confirmed by testing it on actual samples (tap water) using the spike and recovery method. The samples were intentionally contaminated with different quantities of Cu^{2+} ions and then analysed using the newly developed technique. The experiment was repeated up to three times, and the obtained results in the actual samples demonstrated good recognition and recovery of Cu^{2+} ions. This is confirmed by the Table 1, which authenticate its practical and visual relevance for the recognition of Cu^{2+} ions in genuine samples.

Fig. 17 Strip dipped in acetonitrile solution of L with increasing conc. of Cu^{2+} (0 to 100 ppm from left to right).

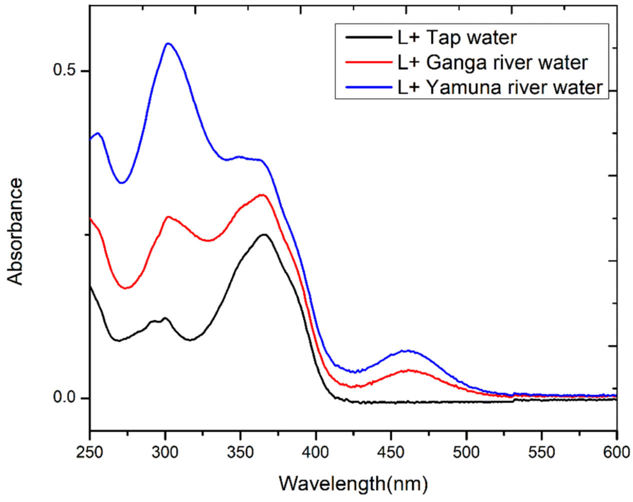

Fig. 18 Showing presence of Cu^{2+} in river water samples.

Table 1 Detection results of Cu^{2+} ions in tap water samples by probe L[a]

Sample	Cu^{2+} ions spiked (μM)	Cu^{2+} ions found ($n = 3$)*	Recovery of Cu^{2+} ions added (%)
Tap water	5	4.93	98.6
	10	10.10	101
	15	14.97	99.8
	20	19.89	99.45

[a] *n = Number of trials.

4.4 Reversibility and molecular logic gate behavior of chemosensor L

Another quality that makes chemosensors attractive for practical applications is their recyclability. EDTA was added to the **L–Cu^{2+}** solution to investigate the **L** recyclability. Owing to the reversible interaction between the **L–Cu^{2+}** complex and EDTA, the absorbance intensity changed when EDTA (0–1 equiv.) was added to the **L–Cu^{2+}** solution. EDTA is an example of a metal ion chelator. It can form a complex with **Cu^{2+}** and easily eliminate it from the complex when introduced into the **L–Cu^{2+}** solution. With the addition of EDTA, the hue changed from yellow to colorless, which could also be observed with the naked eye. The addition of 1 equiv. of EDTA completely bleached the hue of the **L–Cu^{2+}** solution. Following the addition of 0–1 equivalents of EDTA, the shift in the UV-vis absorbance spectra also revealed a decrease in the intensity of the complex band, as shown in Fig. 19.

An interesting application of chemosensors has been observed in the fields of molecular keypad locks, information storage devices, and molecular logic gates. The absorbance reversible switching process of chemosensor **L** can be used for the construction of a molecular logic gate. An 'INHIBIT' molecular logic gate is constructed by using two logic operations of NOT and functions. This is highly important because of its non-commutative behavior, that is, its output signal is inhibited by only one type of input. Therefore, we have used 'INHIBIT' logic gate to explain the practical utility of chemosenor **L** on addition of metal ion Cu^{2+} and EDTA.

Chemical information is encoded into optical signals by an "INHIBIT" logic gate. The absorbance response at 462 nm was used as the output, and two chemical inputs, Cu^{2+} and EDTA, were designated IN 1 and IN 2, respectively.

As shown in Fig. 20, the truth table was created based on the absorbance data using binary digits as input. In this approach, Cu^{2+} and EDTA are represented as '1' and '0', respectively, depending on whether they are chemical inputs. Strong

Table 2 Comparison of reported work with present work

S. No.	Sensors	Cu^{2+} (LOD)	Binding stoichiometric ratio	Ref.
1	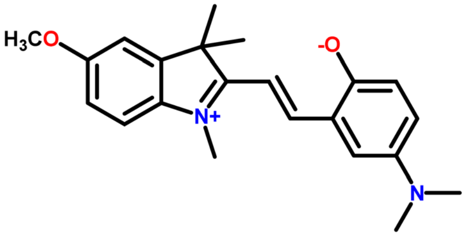	0.11 μM	1 : 1	34
2	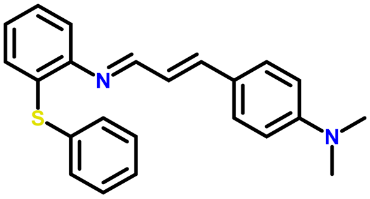	2.85 μM	2 : 1	35
3	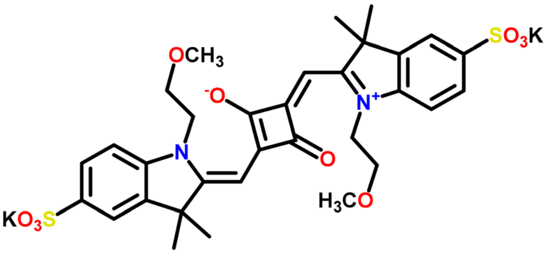	0.188 μM	1 : 2	36
4	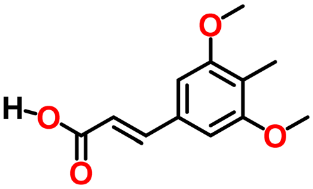	64 nM	1 : 2	37
5	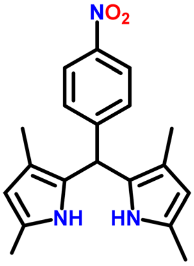	2.51 μM	1 : 2	38
6	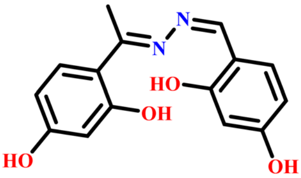	42.09 nM	1 : 1	Our work

absorbance intensity during the signaling process was designated as '1' for output and weak absorbance intensity as '0' for output. The other three input combinations, namely IN 1 = 0′ and IN 2 = 0′, IN 1 = 0′ and IN 2 = 1, IN 1 = 1, and IN 2 = 1, exhibited weak absorbance and 0 was the output. The input combination IN 1 = 1 and IN 2 = 0 indicates a strong absorbance intensity and '1' in the output.

The construction of the "INHIBIT" logic gate for the reversible chemosensor **L** in the presence of Cu^{2+} and the absence of EDTA was thus demonstrated by the above information, which was seen by the UV-vis absorbance response.

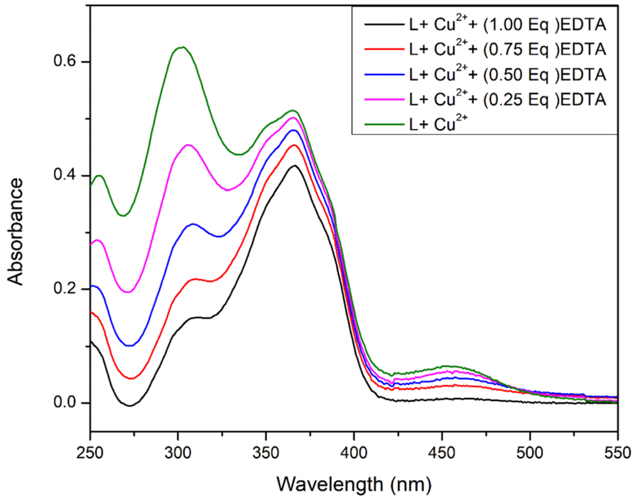

Fig. 19 Absorbance spectra of the reversibility of L–Cu^{2+} upon addition of EDTA.

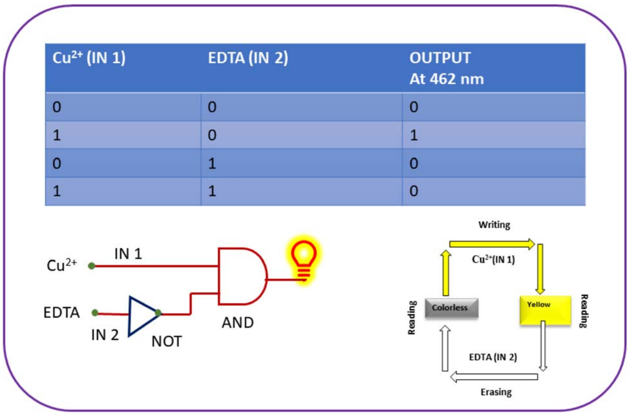

Cu^{2+} (IN 1)	EDTA (IN 2)	OUTPUT At 462 nm
0	0	0
1	0	1
0	1	0
1	1	0

Fig. 20 Schematic representation of the reversible logic operation for the memory element with "write-read-erase-read" operations using the "INHIBIT" logic gate and its truth table based on Cu^{2+} and EDTA.

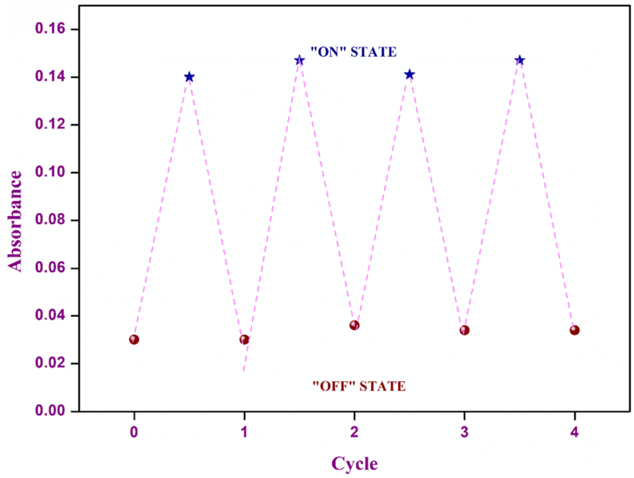

Fig. 21 The reversible and reproducible the absorbance switch controlled by alternating addition of Cu^{2+} and EDTA into the probe (L) solution.

To build memory devices, IN 1 (Cu^{2+}) and IN 2 (EDTA) were employed as two inputs. The system writes and stores binary state 1 when IN 1 = 1 and IN 2 = 0. The system memorizes binary state 1 and writes when it receives IN 1 (Cu^{2+}), which exhibits strong absorbance intensity. However, when IN 2 (EDTA) is present, it erases the data and remembers the binary state 0 or low absorbance. To illustrate the "write-read-erase-read" functions of a sequential logic circuit, we applied a binary-logic function, as illustrated in Fig. 20 and 21.

5. Conclusions

The Schiff base **L** was found to be a successful probe for cupric ion identification in contrast to the other metal ions. The absorption experiments revealed that the synthesized chemosensor **L** had a greater affinity for cupric ions exhibiting a binding constant of 3.022×10^4 M^{-1} and limit of detection to be 42.09 nM. To validate the experimental results, computational studies were performed. In addition, **L** replicates the INHIBIT molecular logic gate and demonstrates reversible switching for Cu^{2+} upon the addition of EDTA to the solution of **L–Cu^{2+}**, confirming that this chemosensor is reusable. The chemosensor demonstrated its practical utility by successfully detecting Cu^{2+} ions in both solid state and filter paper strips. DFT computations revealed that the interaction of **L** with Cu^{2+} resulted in a robust complex, where the Cu^{2+} ions interacted with three atoms of the ligand **L**. The coordination of the Cu^{2+} ion with the nitrogen atom of the imine group and two oxygen atoms of the hydroxyl group elucidated the complex's characteristics. Further, the docking studies for ligand **L** revealed a remarkable binding affinity with human hemoglobin, revealing information on its favorable binding positions within hemoglobin binding sites and the subsequent interactions with HHb. These findings highlight ligand **L** as a prospective candidate for further investigations in the design of novel therapeutic strategies and development for hemoglobin-related diseases.

Data availability

The data supporting this article have been included in the ESI.† This CCDC for **L**: 2296396 contains ESI† crystallographic data for ligand in this study.

Conflicts of interest

The authors declare that they have no conflicts of interest.

Acknowledgements

Ram Kumar is grateful to Bhaskaracharya College of Applied Sciences, University of Delhi for providing research facilities, University of Delhi for financial support and the University Science Instrumentation Centre (USIC) for characterization facilities and also very grateful to single crystal operator Sanjay sir. All the authors are thankful to the Department of Chemistry, University of Delhi.

References

1 J. J. DiNicolantonio, D. Mangan and J. H. O'Keefe, *Open heart*, 2018, **5**, e000784.
2 H. Tapiero, D. M. Townsend and K. D. Tew, *Biomed. Pharmacother.*, 2003, **57**, 386–398.
3 E. Gaggelli, H. Kozlowski, D. Valensin and G. Valensin, *Chem. Rev.*, 2006, **106**, 1995–2044.
4 A. M. Elkhatat, M. Soliman, R. Ismail, S. Ahmed, N. Abounahia, S. Mubashir, S. Fouladi and M. Khraisheh, *Bull. Natl. Res. Cent.*, 2021, **45**, 1–18.
5 S. Bayindir, A. S. Hussein, F. Lafzi and M. Toprak, *J. Mol. Liq.*, 2023, **382**, 121939.
6 F.-C. Ho, Y.-J. Huang, C.-C. Weng, C.-H. Wu, Y.-K. Li, J. I. Wu and H.-C. Lin, *ACS Appl. Mater. Interfaces*, 2020, **12**, 53257–53273.
7 F. Wang, R. Nandhakumar, J. H. Moon, K. M. Kim, J. Y. Lee and J. Yoon, *Inorg. Chem.*, 2011, **50**, 2240–2245.
8 E. Manandhar, J. H. Broome, J. Myrick, W. Lagrone, P. J. Cragg and K. J. Wallace, *Chem. Commun.*, 2011, **47**, 8796–8798.
9 R. Kumar, B. Singh, P. Gahlyan, R. Kumar and B. Pani, *J. Mol. Struct.*, 2023, 135859.
10 X. Wang, G. Liu, Y. Qi, Y. Yuan, J. Gao, X. Luo and T. Yang, *Anal. Chem.*, 2019, **91**, 12006–12013.
11 M. T. Feroze, D. Doonyapisut, B. Kim and C.-H. Chung, *Korean J. Chem. Eng.*, 2023, **40**, 1014–1022.
12 R. Cai, C. A. Shoukat, C. Zhang, X. Gao, H. Li, J. Chen, Y. Ji and X. Wu, *Analyst*, 2023, **148**, 3306–3311.
13 M. H. Chua, H. Zhou, Q. Zhu, B. Z. Tang and J. W. Xu, *Mater. Chem. Front.*, 2021, **5**, 659–708.
14 R. Kumar, B. Singh, S. S. Pandey and B. Pani, *SynOpen*, 2023, **7**, 703–717.
15 P. V Mane, P. Patil, A. A. Mahishi, M. Kigga, M. P. Bhat, K.-H. Lee and M. Kurkuri, *Heliyon*, 2023, **9**(6), DOI: **10.1016/j.heliyon.2023.e16600**.
16 P. Sengupta, A. Ganguly and A. Bose, *Spectrochim. Acta, Part A*, 2018, **198**, 204–211.
17 P. Patil, M. Prasad, M. P. Bhat, M. G. Gatti, S. Kabiri, T. Altalhi, H.-Y. Jung, D. Losic and M. Kurkuri, *Chem. Eng. J.*, 2017, **327**, 725–733.
18 A. Beylot and J. Villeneuve, *Resour. Policy*, 2015, **44**, 161–165.
19 C.-L. Huang, M. Xu, S. Cui, Z. Li, H. Fang and P. Wang, *Resour., Conserv. Recycl.*, 2020, **161**, 104861.
20 M. Mróz, *Energies*, 2022, **15**, 560.
21 D. Peukert, C. Xu and P. Dowd, *Minerals*, 2022, **12**, 1364.
22 S. E. Crawford, P. R. Ohodnicki and J. P. Baltrus, *J. Mater. Chem. C*, 2020, **8**, 7975–8006.
23 G. M. Sheldrick, *Acta Crystallogr., Sect. C: Struct. Chem.*, 2015, **71**, 3–8.
24 O. V Dolomanov, L. J. Bourhis, R. J. Gildea, J. A. K. Howard and H. Puschmann, *J. Appl. Crystallogr.*, 2009, **42**, 339–341.
25 C. F. Macrae, P. R. Edgington, P. McCabe, E. Pidcock, G. P. Shields, R. Taylor, M. Towler and J. V. D. Streek, *J. Appl. Crystallogr.*, 2006, **39**, 453–457.
26 S. Yu, in *Blood Substitutes and Oxygen Biotherapeutics*, Springer, 2022, pp. 45–51.
27 O. Trott and A. J. Olson, *J. Comput. Chem.*, 2010, **31**, 455–461.
28 A. I. Said, N. I. Georgiev and V. B. Bojinov, *J. Photochem. Photobiol., A*, 2015, **311**, 16–24.
29 R. Bauernschmitt and R. Ahlrichs, *Chem. Phys. Lett.*, 1996, **256**, 454–464.
30 M. E. Casida, C. Jamorski, K. C. Casida and D. R. Salahub, *J. Chem. Phys.*, 1998, **108**, 4439–4449.
31 R. E. Stratmann, G. E. Scuseria and M. J. Frisch, *J. Chem. Phys.*, 1998, **109**, 8218–8224.
32 G. Scalmani, M. J. Frisch, B. Mennucci, J. Tomasi, R. Cammi and V. Barone, *J. Chem. Phys.*, 2006, **124**, DOI: **10.1063/1.2173258**.
33 F. Furche and R. Ahlrichs, *J. Chem. Phys.*, 2002, **117**, 7433–7447.
34 K. M. Trevino, B. K. Tautges, R. Kapre, F. C. Franco Jr, V. W. Or, E. I. Balmond, J. T. Shaw, J. Garcia and A. Y. Louie, *ACS Omega*, 2021, **6**, 10776–10789.
35 Z. Aydin and M. Keles, *ChemistrySelect*, 2020, **5**, 7375–7381.
36 Y. Liu, L. Wang, C. Guo and Y. Hou, *Tetrahedron Lett.*, 2018, **59**, 3930–3933.
37 P. Sengupta, A. Ganguly and A. Bose, *Spectrochim. Acta, Part A*, 2018, **198**, 204–211.
38 K. Rajaswathi, M. Jayanthi, R. Rajmohan, V. Anbazhagan and P. Vairaprakash, *Spectrochim. Acta, Part A*, 2019, **212**, 308–314.